Received September 2002
Accepted January 2003

Modeling of convection enhancement mechanisms

G. Comini, G. Croce and C. Nonino
Dipartimento di Energetica e Macchine, Università degli Studi di Udine, Udine, Italy

Keywords *Convection, Surface conductivity, Transverse waves, Finite element analysis*

Abstract *Most compact heat exchangers and heat dissipating components rely on convection enhancement mechanisms that reduce the continuous growth of boundary layers. Usually surface irregularities, in the form of interruptions and/or vortex generators, are introduced in the flow passages. The resulting geometric configurations are periodic in space and, after a short distance from the entrance, induce velocity and thermal fields that repeat themselves from module to module. The numerical models presented here consider the space-periodicity and allow flows that are stationary at sub-critical values of the Reynolds number, but become time-periodic, or quasi periodic, above the critical value of the Reynolds number. Space discretizations are achieved by an equal order finite element procedure based on a projection algorithm. Two-dimensional schematizations are employed to analyze the effects of surface interruptions and transverse vortex generators, while three-dimensional schematizations are employed for longitudinal vortex generators.*

Nomenclature

$\mathbf{a}$	= vector of nodal values of a
a	= independent variable
A	= amplitude
D_h	= hydraulic diameter
f	= Fanning friction factor
h	= average convection coefficient
H	= height of the channel, measured in the z-direction
$\mathbf{H}$	= effective stiffness matrix
k	= thermal conductivity
L	= length, measured in the x-direction
$\mathbf{n}$	= outward oriented normal to the external surface
$\mathbf{N}$	= vector of interpolating functions
Nu	= average Nusselt number
p	= pressure
$\tilde{p}$	= periodic component of pressure
q	= heat flow rate
Pr	= Prandtl number
Re	= Reynolds number
S	= surface
St	= Strouhal number
t	= temperature
T	= dimensionless temperature
u, v, w	= velocity components in the (x, y, z) directions
$\mathbf{v}$	= velocity vector
W	= width of the channel, measured in the y-direction
x, y, z	= Cartesian coordinates
α	= average pressure gradient in the flow direction x
μ	= dynamic viscosity
ϑ	= time
Θ	= period
ρ	= density

Subscripts

b	= bulk
lm	= logarithmic mean
Nu	= associated with the Nusselt number
w	= wall
0	= associated with the corresponding smooth duct

International Journal of Numerical Methods for Heat & Fluid Flow
Vol. 14 No. 1, 2004
pp. 66-84

0961-5539
DOI 10.1108/09615530410511630

Introduction

Convection enhancement is needed to obtain more compact and less expensive heat exchangers or to decrease thermal resistances in heat dissipating components (Kays and London, 1984; Shah and Bhatti, 1987; Webb, 1987, 1994) As pointed out by Fiebig (1996), the enhancement of convection is most effectively achieved by limiting the continuous growth of boundary layers through periodical interruptions, separations and destabilizations. For this purpose, extensive use is made of specially configured devices, in the form of offset-strip surfaces, wavy channels, louvered fins, winglets and ribs. Offset-strip and louvered surfaces mainly rely on restarts of boundary layers in order to reduce thermal resistances with respect to continuous plates (Heikal *et al.*, 2000; Zhang *et al.*, 1997). Wavy channels, winglets and ribs mainly rely on the generation of vortices that interfere with the growth of boundary layers by separating and, eventually, destabilizing them. Ali and Ramadhyani (1992) presented a review of convection enhancement by wavy surfaces, while Fiebig and Mitra (1998) presented a review of convection enhancement by winglets. In the literature, many data are also available for convection enhancement by transverse and angled ribs (Cheung and Huang, 1991; Kukreja *et al.*, 1993; Lopez *et al.*, 1996; Sundén, 1999; Webb and Ramadhyani, 1985). The bulk of these studies shows that, in order to reduce thermal resistances, vortices must not only separate but also recirculate the fluid between core and wall regions of the flow passages. This is very often the case with longitudinal vortices. On the contrary, transverse vortices do not produce significant mixing until flows become unsteady above a critical Reynolds number. Only then, self-sustained flow oscillations periodically move transverse vortices upstream and downstream, bringing fresh fluid from the core to the walls.

Many numerical investigations of convection enhancing mechanisms have been carried out, following the pioneering work of Kelkar and Patankar (1987) and Patankar *et al.* (1977). In particular, the finite-element approach, introduced by Nonino and Comini (1998), has been applied successfully by Comini and Croce (2001) and Comini *et al.* (2002) to the analysis of tube-fin exchangers, and by Nonino and Comini (2002) to the analysis of ribbed channels. The purpose of this paper is the illustration of modeling procedures, rather than the production of exhaustive databases of numerical results. In this context, two-dimensional schematizations are used for surface interruptions and transverse vortex generators, while three-dimensional schematizations are employed for longitudinal vortex generators. Flows are always laminar, even if they become unsteady above the critical value of the Reynolds number corresponding to the onset of self-sustained oscillations. As a consequence, time-dependent models are utilized in all the simulations.

Statement of the problem

The geometries considered in this study are made up of the repetition of identical modules. After a short distance from the entrance, flow and thermal fields repeat themselves from module to module attaining a fully developed character. In the two-dimensional schematization of Figure 1 we consider a wavy channel with an infinite aspect ratio (width W over height H). The repetitive fields allow the limitation of the analysis to a single module, such as the one enclosed by the periodic boundaries S_1 and S_2. On the other hand, it is possible to reduce the computational domain still further by considering only one half of the module such as, for example, the one enclosed by the anti-periodic boundaries S_1 and S_3.

In the three-dimensional schematizations of Figure 2, we consider ribbed channels with square cross sections. The rib distribution can be one-sided or staggered, while the ribs can be transverse (90°), or variously angled. When the ribs are one-sided, we can easily identify two periodic boundaries, such as S_1 and S_2. When the ribs are staggered, we can refer to the anti-periodic boundaries S_1 and S_3. At periodic boundaries S_1 and S_2, distributions of velocity components and dimensionless temperatures are periodic functions. At anti-periodic boundaries S_1 and S_3, the relationships between velocity components and dimensionless temperatures must be expressed by anti-periodic functions.

Flow and temperature fields

Assuming the thermophysical properties of the fluid to be constant and the flow to be laminar, the governing equations are the standard Navier-Stokes and continuity equations. They can be expressed as

$$\rho \frac{\partial \mathbf{v}}{\partial \vartheta} + \rho \mathbf{v} \cdot \nabla \mathbf{v} = \mu \nabla^2 \mathbf{v} - \nabla p \tag{1}$$

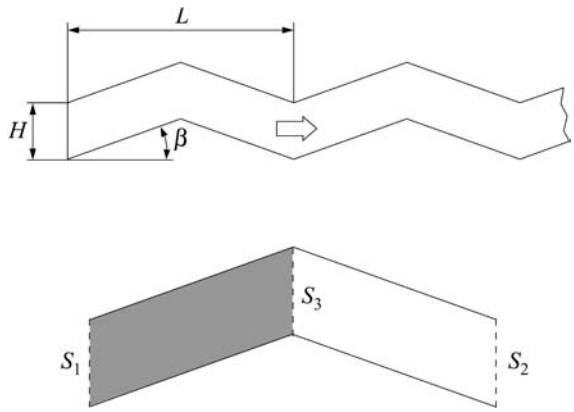

Figure 1.
Two-dimensional wavy channels: schematic representation of the geometry and periodic (S_1 and S_2), and anti-periodic (S_1 and S_3) boundaries in the computational cell

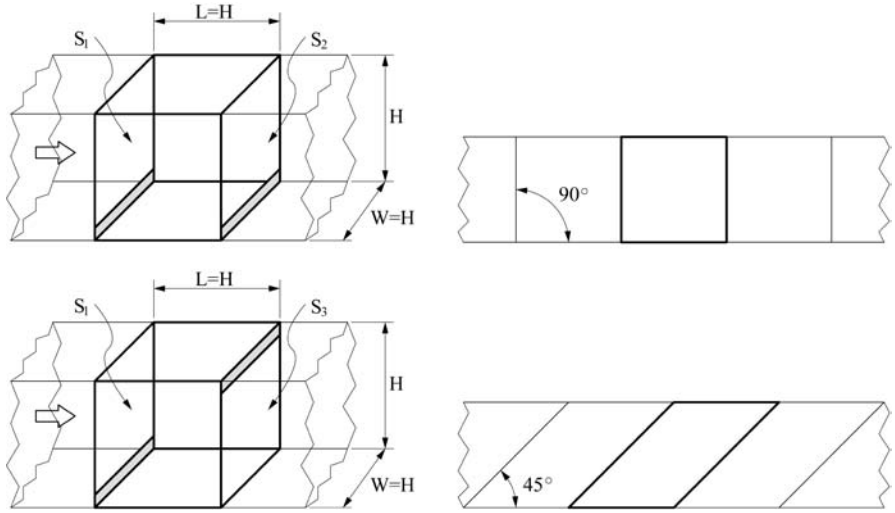

Figure 2.
Ribbed square channels: periodic boundaries (S_1 and S_2) with one-sided ribs, anti-periodic boundaries (S_1 and S_3) with staggered ribs; traces of transverse (90° ribs) and 45° ribs

$$\nabla \cdot \mathbf{v} = 0 \tag{2}$$

In the above equations, $\mathbf{v}$ is the velocity vector, ϑ the time, ρ the density, μ the dynamic viscosity, and p the deviation from the hydrostatic pressure. In the absence of volumetric heating and neglecting the effects of viscous dissipation, the energy equation can be written as

$$\rho c \frac{\partial t}{\partial \vartheta} + \rho c \mathbf{v} \cdot \nabla t = k \nabla^2 t \tag{3}$$

where c is the specific heat and k the thermal conductivity.

In a periodic fully developed flow, the pressure p can be expressed as the sum of a linear term, accounting for the average pressure gradient, and a residual term that behaves in a periodic manner. Thus, we have

$$p = -\alpha x + \tilde{p} \tag{4}$$

where α is a constant representing the average pressure gradient in the flow direction x and $\tilde{p}$ is the periodic component. With reference to three-dimensional schematizations of Figure 2, the symmetric periodicity of $\tilde{p}$ between boundaries S_1 and S_2 leads to the condition

$$\tilde{p}(L, y, z) = \tilde{p}(0, y, z) \tag{5}$$

while the antisymmetric periodicity between boundaries S_1 and S_3 yields the condition

$$\tilde{p}(L, y, H - z) = \tilde{p}(0, y, z) \tag{6}$$

In the above equations, z is the distance from the bottom boundary measured in the vertical direction and H is the height of the channel.

Appropriate conditions must be specified at wall and periodic boundaries. At wall boundaries, the no-slip condition holds well

$$u = v = w = 0 \tag{7}$$

At periodic boundaries, the symmetric periodicity between S_1 and S_2 leads to the conditions

$$\begin{aligned} u(L, y, z) &= u(0, y, z) \\ v(L, y, z) &= v(0, y, z) \\ w(L, y, z) &= w(0, y, z) \end{aligned} \tag{8}$$

while the antisymmetric periodicity between S_1 and S_3 leads to the conditions

$$\begin{aligned} u(L, y, H - z) &= u(0, y, z) \\ v(L, y, H - z) &= v(0, y, z) \\ w(L, y, H - z) &= w(0, y, z) \end{aligned} \tag{9}$$

Conditions (8) and (9) do not involve the specification of any inflow velocities. To obtain the desired value of the average velocity on the cross section S, the pressure gradient α must be adjusted iteratively as described, for example, by Nonino and Comini (1998)

$$\bar{u} = \frac{1}{S} \int_S u \, \mathrm{d}S \tag{10}$$

The behavior of the flow is determined by the Reynolds number

$$\mathrm{Re} = \frac{\rho \bar{u} D_\mathrm{h}}{\mu} \tag{11}$$

and can be characterized, for example, by the Fanning friction factor

$$f = \frac{\alpha D_\mathrm{h}}{2\rho \bar{u}^2} \tag{12}$$

which is directly related to the pressure gradient α. In equations (11) and (12), we use the hydraulic diameter D_h to compare performances of different surface configurations. However, the Reynolds number for discontinuous fins is often

evaluated on the basis of the projected length of a single module (Kays and London, 1984; Shah and Bhatti, 1987).

The wall boundary condition utilized for temperature is

$$t = t_w = \text{const.} \tag{13}$$

As pointed out by Kelkar and Patankar (1987) and Nonino and Comini (1998), the periodicity conditions are applied to the dimensionless temperature

$$T = \frac{t - t_w}{t_b - t_w} \tag{14}$$

where t_b is the bulk temperature defined as

$$t_b = \frac{\int_{S'} |\mathbf{v} \cdot \mathbf{n}| t \, dS}{\int_{S'} |\mathbf{v} \cdot \mathbf{n}| \, dS} \tag{15}$$

while S' is the area of the surface parallel to the inflow/outflow boundaries, and $\mathbf{n}$ is the unit vector normal to the surface.

The symmetric periodicity of T between boundaries S_1 and S_2 in Figure 2 leads to the condition

$$\frac{t(L,y,z) - t_w}{t_b(L) - t_w} = \frac{t(0,y,z) - t_w}{t_b(0) - t_w} \tag{16}$$

since T identically repeats itself from module to module. Equation (16) can be written in the form

$$t(L,y,z) = \left[1 + \frac{t_b(L) - t_b(0)}{t_b(0) - t_w}\right] t(0,y,z) - \frac{t_b(L) - t_b(0)}{t_b(0) - t_w} t_w \tag{17}$$

Similarly, the antisymmetric periodicity between boundaries S_1 and S_3 in Figure 2 leads to the condition

$$\frac{t(L,y,H-z) - t_w}{t_b(L) - t_w} = \frac{t(0,y,z) - t_w}{t_b(0) - t_w} \tag{18}$$

which can be written in the form

$$t(L,y,H-z) = \left[1 + \frac{t_b(L) - t_b(0)}{t_b(0) - t_w}\right] t(0,y,z) - \frac{t_b(L) - t_b(0)}{t_b(0) - t_w} t_w \tag{19}$$

Equations (17) and (19) contain two unknown quantities: the bulk temperature at inflow $t_b(0)$ and the difference between the bulk temperatures at outflow and inflow. However, in the solution process we can first impose the value of the

difference in the bulk temperatures, and then we can iterate until convergence is reached for a value of $t_b(0)$ which verifies the periodicity condition.

The average Nusselt number is defined as

$$\mathrm{Nu} = \frac{hD_h}{k} \tag{20}$$

where

$$h = \frac{q}{S_0 \overline{\Delta t}} \tag{21}$$

is the average heat transfer coefficient, S_0 is the heat transfer surface pertaining to the corresponding module of a smooth channel, q is the total heat flow rate and

$$\overline{\Delta t} = \Delta t_{lm} = \frac{[t_w - t_b(L)] - [t_w - t_b(0)]}{\ln\{[t_w - t_b(L)]/[t_w - t_b(0)]\}} \tag{22}$$

is the logarithmic mean temperature difference.

It must be pointed out that the above presentation holds well also for the two-dimensional case, provided that the y-coordinate is neglected in the equations.

Numerical solution

The momentum, continuity and energy equations are solved by an equal-order, finite-element procedure based on the projection algorithm illustrated by Nonino and Comini (1997) and Nonino *et al.* (1999). At each time step, a pseudovelocity field is obtained by neglecting the pressure gradients in the momentum equations. Then, by enforcing continuity on the pseudo-velocity field, a tentative pressure is estimated and the momentum equations are solved for the tentative velocity field. Afterwards, continuity is enforced again to find pressure corrections. Pressure corrections are also used to find the velocity corrections that project the tentative velocity field onto a divergence-free space. Once the velocity field has been found, the energy equation can be solved before moving to the next step.

The momentum and energy equations are considered as particular versions of the transport equation for a generic dependent variable a. This equation is written in the time-discretized form

$$\gamma \frac{a^{n+1} - a^n}{\Delta \vartheta} + \gamma \mathbf{v}^n \cdot [\tau_v \nabla a^{n+1} + (1 - \tau_v) \nabla a^n]$$
$$= \Gamma[\tau_\Gamma \nabla^2 a^{n+1} + (1 - \tau_\Gamma) \nabla^2 a^n] + \dot{s} \tag{23}$$

where the properties γ and Γ, and the volumetric source rate $\dot{s}$ are identified by inspection of the appropriate original equations. The weighting factors

τ_v and τ_Γ, both in the range from 0 to 1, allow the selection of different time-integration schemes. The pressure and the pressure correction equations are particular versions of the Poisson equation, which can be obtained from equation (23) by assuming $\gamma = 0$ and $\tau_\Gamma = \Gamma = 1$.

The space discretization of equation (23) is based on the Bubnov-Galerkin method, avoiding the use of upwinding. The unknown functions are approximated by the expansions

$$a = \sum N_j a_j = \mathbf{Na} \tag{24}$$

where a_j stand for the nodal values, while N_j are the interpolating/weighting functions. Substituting equation (24) into the appropriate weak forms, yields systems of space discretized equations that can be written as

$$\mathbf{Ha} = \mathbf{g} \tag{25}$$

where **a** is the vector of nodal values, **H** is the effective stiffness matrix considering all homogeneous contributions, and **g** is the effective load vector, considering all non-homogeneous contributions. The periodic boundary conditions are introduced as illustrated in detail by Comini *et al.* (2002) and Nonino and Comini (2002). In particular, it must be noticed that, with reference to the corresponding points on the inflow (i) and outflow (o) boundaries, all the periodic boundary conditions can be expressed in the general form

$$a_\mathrm{o} = Ba_\mathrm{i} + D \tag{26}$$

where the values of B and D can be easily inferred from the physical boundary conditions. Accordingly, the matrix **H** and the right hand side vector **g** in equation (25) are modified to consider equation (26).

In the numerical simulations, iterative algorithms were used to solve the systems of linear equations arising at each time step from the discretization process. The conjugate gradient squared (CGS) method, described by Howard *et al.* (1990), was used to solve the discretized momentum and energy equations. The modified conjugate gradient (MCG) method, illustrated by Gambolati (1988, p. 136) was used to solve the symmetric systems obtained from the discretization of the Poisson equations. In both cases, preconditioned matrices were obtained from an incomplete LU decomposition (ILU).

Results and discussion

For the sake of simplicity, in the simulations we assumed negligible thickness and infinite thermal conductivity of the fins. The solutions illustrated here concern laminar flows of air ($\mathrm{PR} = 0.7$) that range from stationary to time-periodic and quasi-periodic. In time-periodic or quasi-periodic situations, mean parameters were further averaged over a period or a suitable interval of time, to have single representative values. Therefore, we obtained

$$\langle \varphi \rangle = \frac{1}{\Theta} \int_{\vartheta}^{\vartheta+\Theta} \varphi(\vartheta)\, \mathrm{d}\vartheta \tag{27}$$

where $\varphi = f,\ \mathrm{Nu}$. On the other hand, to lighten the notation, the symbol $\langle\ \rangle$ will be omitted in the following.

Surface interruptions

As already pointed out, surface interruptions limit the growth of boundary layers through periodical restarts. In Figure 3, we focus on a typical geometry belonging to the category of the offset-strip channels that can be found in tube-fin heat exchangers. By simplifying the flow in an actual tube-fin exchanger to a channel flow between parallel plates, we neglect the presence of transverse tubes. However, we can still adequately consider the fins influence as far as the renovation of boundary layers is concerned.

In the computational cell shown in Figure 3, we can easily identify two "standard" antiperiodic boundaries S_1 and S_3, and two periodic boundaries S_4 and S_5, where corresponding points are characterized by the same values of the x-coordinate. At corresponding points on S_4 and S_5 we have not only the same velocities, but also the same temperatures.

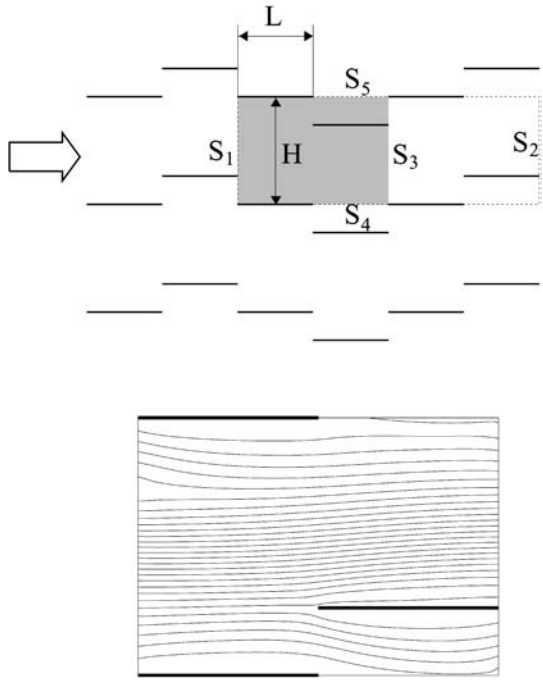

Figure 3.
Offset-strip channels: computational cell and steady state contours of streamlines at Re = 300

$$t(x, H) = t(x, 0) \tag{28}$$

Streamline contours for two-dimensional flows through offset-strip fins at Re = 300 are also represented in Figure 3. At such a relatively low Reynolds number, the flow is regular and steady as in flat channels. However, with respect to flat channels, we have substantial increases in both the pressure drop and heat transfer rate, because of the renovation of boundary layers. This behavior can be seen clearly in Figure 4 where the Nu and f values, pertaining to fully developed flows in offset-strip channels, have been divided by the corresponding values for flat channels ($Nu_0 = 7.5407$ and $f_0 = 24.00/Re$) as reported by Shah and Bhatti (1987, p. 3.30). The resulting Nu/Nu_0 values have been denoted by square symbols, while the f/f_0 values have been denoted by triangular symbols. Above the critical value of the Reynolds number ($Re_{cr} \cong 750$), the flow becomes unsteady because transverse vortices, generated at the leading edges, periodically move downstream and leave at the trailing edges. These vortices bring fresh fluid from the main stream to the surface and, consequently, further enhance the local heat transfer coefficients. On the other hand, the influence of transverse vortices will be illustrated in the next paragraph, which deals with two-dimensional wavy channels, where the effects of surface interruptions are not superimposed.

Transverse vortices

Transverse vortices, i.e. vortices whose axis of rotation is normal to the main flow, can be found in most compact heat exchangers where specially configured surfaces are utilised as transverse vortex generators. For this purpose, wavy channels have been extensively employed in the past, and are still preferred in many low-cost applications. The geometry considered has already been shown in Figure 1.

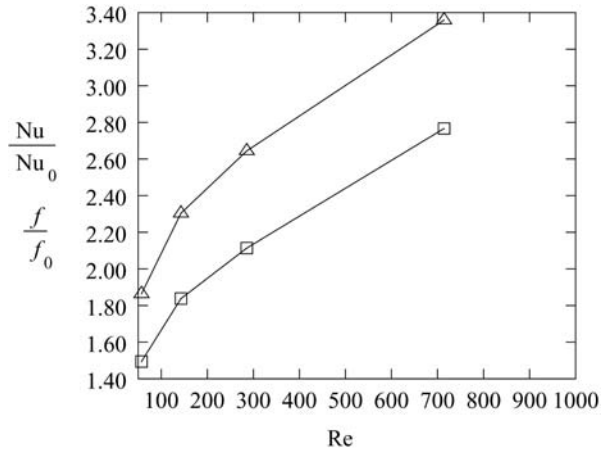

Figure 4.
Offset-strip channels: Fanning friction factors (triangles) and average Nusselt numbers (squares) for $Re < Re_{cr}$ normalized with corresponding values for flat channels

Streamline contours for the flow in a two-dimensional wavy channel are reported in Figure 5. At Re = 100, the streamline contours demonstrate that the flow is quite regular and steady. In this case, heat transfer enhancements with respect to flat channels are only due to the increase of the exchange surface per unit volume. At Re = 500 and at Re = 1,000 the flow is unsteady and irregular, as demonstrated by the instantaneous representations of streamline contours.

The irregularities in the flow pattern, which increase with the Reynolds number, and the different flow regimes influence both Nusselt numbers and friction factors. However, Figure 6 shows that the values of Nu/Nu_0 (denoted

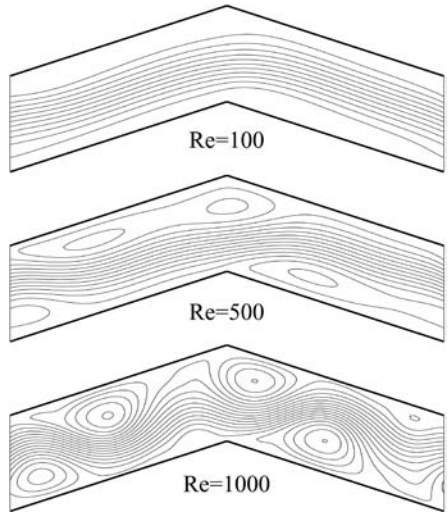

Figure 5.
Two-dimensional wavy channels: steady state contours of streamlines at Re = 100 and instantaneous contours at Re = 500 and 1,000

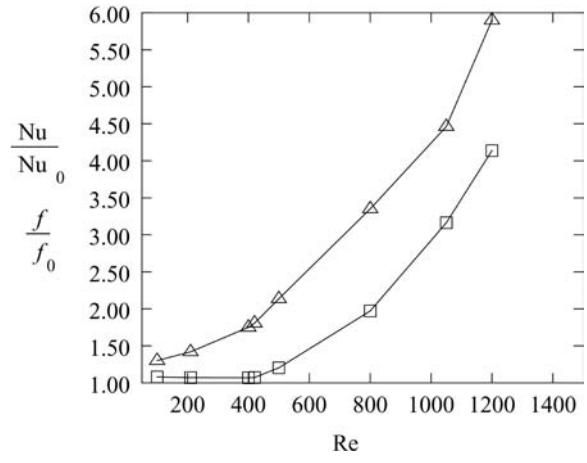

Figure 6.
Two-dimensional wavy channels: Fanning friction factors (triangles) and average Nusselt numbers (squares) normalized with corresponding values for flat channels

by square symbols) remain approximately constant up to the critical Reynolds number ($\mathrm{Re}_{cr} \cong 400$). On the contrary, values of f/f_0 (denoted by triangular symbols) steadily increase, but at a much higher rate above Re_{cr}. As already noted, below the critical value of the Reynolds number, heat transfer enhancements with respect to flat channels are only due to the increase of the exchange surface per unit volume. On the contrary, above the critical value of the Reynolds number, heat transfer enhancements are mainly due to the washing of the channel walls by vortices that detach periodically from the corners and move downstream.

The transport of fluid from the walls to the core, and vice versa, is clearly shown in Figure 7, where travelling vortices for $\mathrm{Re} = 500$ are represented at intervals of one quarter of a period.

The periodic behavior of the heat transfer process is shown in Figure 8. We consider first the time variations of the space-averaged Nusselt number, then the corresponding power density spectra, and finally, the (u, w) phase trajectories at a reference point in the center of the inflow section. The spectra are obtained from the FFT analysis and refer to the peak-to-peak amplitude A_{Nu} of the Nusselt number oscillations. At $\mathrm{Re} = 1,000$ (left column), both the Nu vs ϑ representation and the phase diagram (an irregular but closed curve) indicate that the time behavior is still periodic with one dominant frequency. When expressed in terms of the Strouhal number

$$\mathrm{St} = \frac{D_{\mathrm{h}}}{\Theta \bar{u}} \tag{29}$$

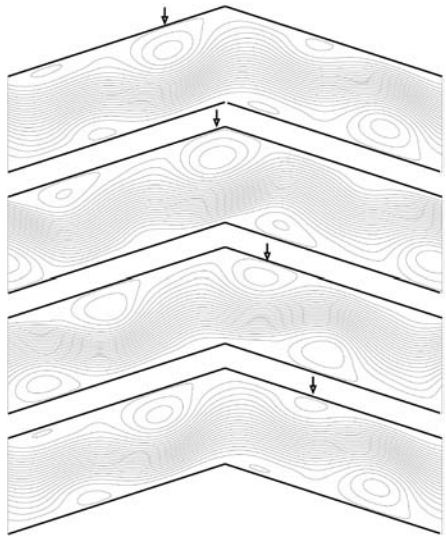

Figure 7.
Two-dimensional wavy channels: streamline patterns for $\mathrm{Re} = 500$ at intervals of one quarter of a period

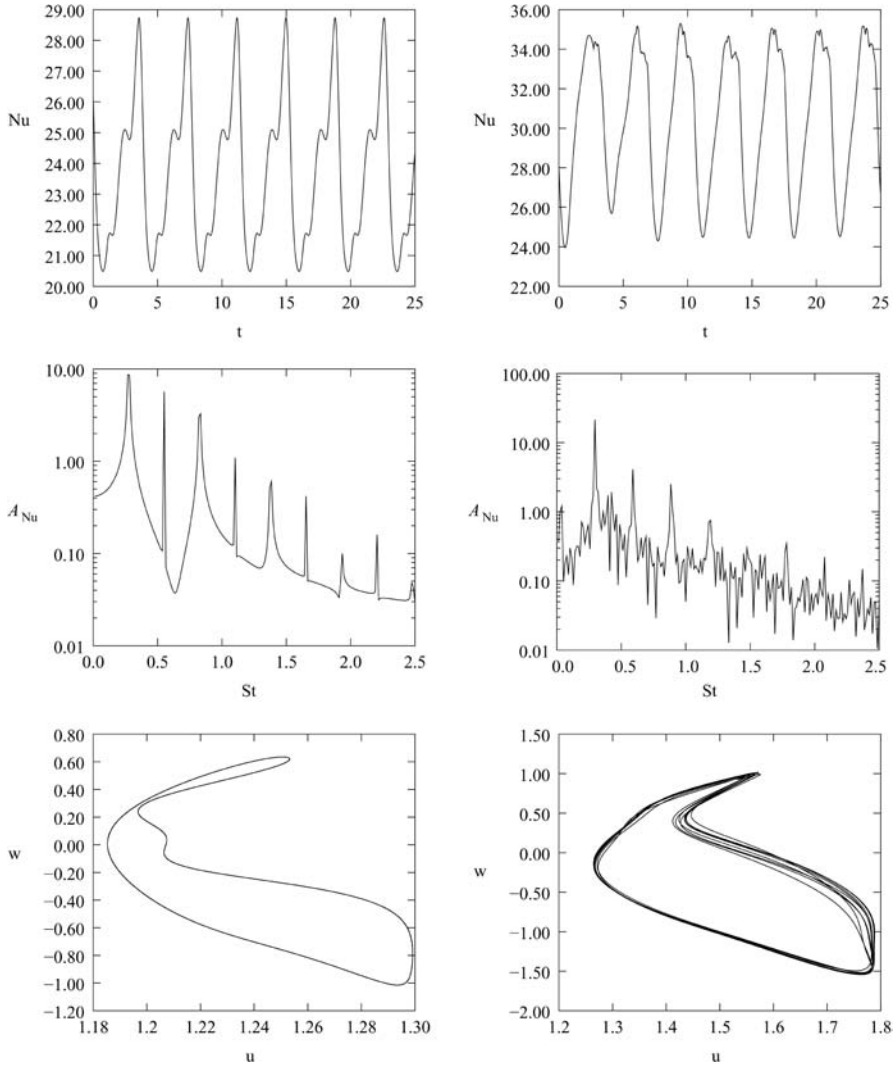

Figure 8.
Two-dimensional wavy channels: time behavior of the space-averaged Nusselt number (top), corresponding power density spectra (centre) and (*u, w*) phase trajectories (bottom), at Re = 1,000 (left), and 1,100 (right)

the dimensionless value of the dominant frequency is St $\cong$ 0.24. At Re = 1,100, the behavior has become quasi-periodic, as can be inferred from the Nu vs ϑ representation. Correspondingly, the Fourier transform shows a quite distributed spectrum over a broad frequency range and the phase diagrams are "almost closed" curves.

Longitudinal vortices

As already pointed out, transverse vortices significantly enhance convection only above the critical Reynolds number. On the contrary, longitudinal

vortices, i.e. vortices whose axis of rotation is aligned with the main flow direction, can produce mixing of fluid from the wall region to the core of the flow, and vice versa, even in stationary conditions.

In a three-dimensional wavy channel of the type shown in Figure 9, longitudinal vortices are known to develop in the vicinity of lateral walls, because of the combined action of centrifugal and viscous forces. Figure 9 shows the characteristics of the flow at Re = 200. As can be seen, the flow is quite regular and steady, with two longitudinal counter-rotating vortices close to the lateral walls. Secondary flows, associated with the longitudinal vortices, clearly move fresh fluid from the walls to the center, and thus, determine an increase of the heat transfer rate.

Longitudinal vortices are also produced by a couple of winglets in a three-dimensional smooth channel. The geometry and the characteristics of such a flow at Re = 350 are shown in Figure 10. Once again, the velocity field is

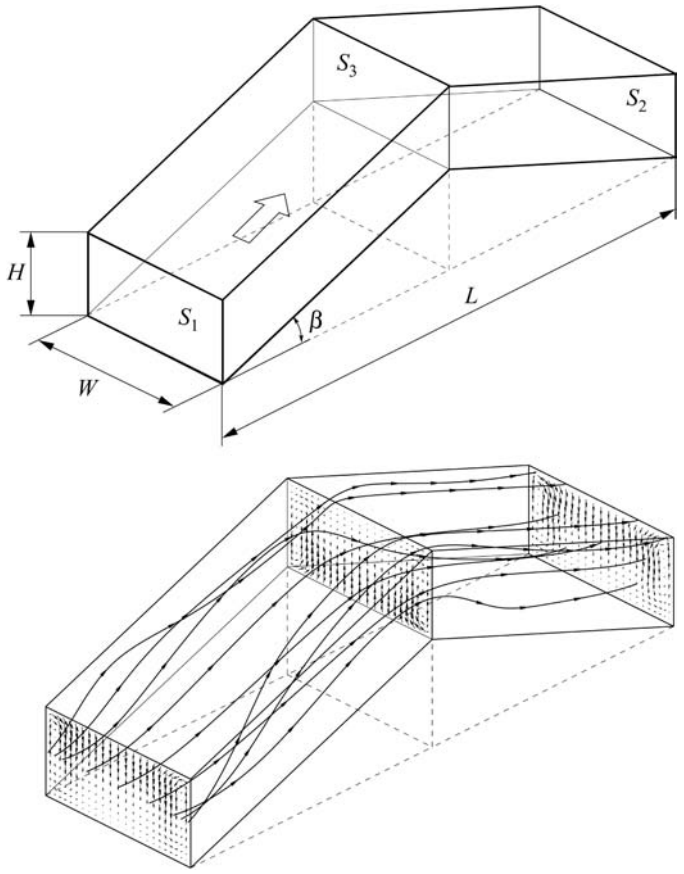

Figure 9.
Three-dimensional wavy channels: computational cell and steady-state trajectories and transverse velocity vectors at Re = 200

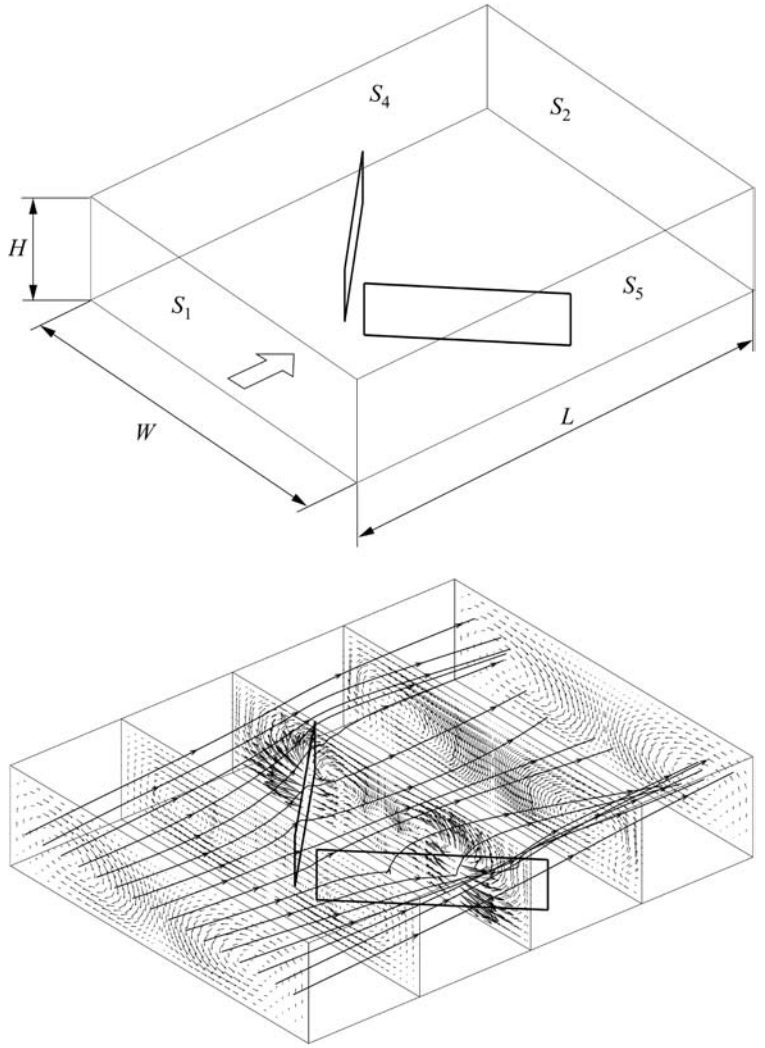

Figure 10.
Wing-type vortex generators: computational cell and steady-state trajectories and transverse velocity vectors at Re = 350

regular and steady, but the two counter-rotating longitudinal vortices move the fluid from the walls to the center.

The influence of longitudinal vortices can be most conveniently illustrated by referring to stationary flows in ribbed channels. The geometries considered have already been represented in Figure 2. At Re = 300, we have stationary flows in all the configurations, and the corresponding fields are shown in Figure 11, where plots of trajectories and velocity vectors are represented. As can be seen, the staggered angled ribs induce two longitudinal counter-rotating vortices, which move the fluid from the region near the walls to the center of the channels. On the contrary, the non-staggered angled ribs induce only one

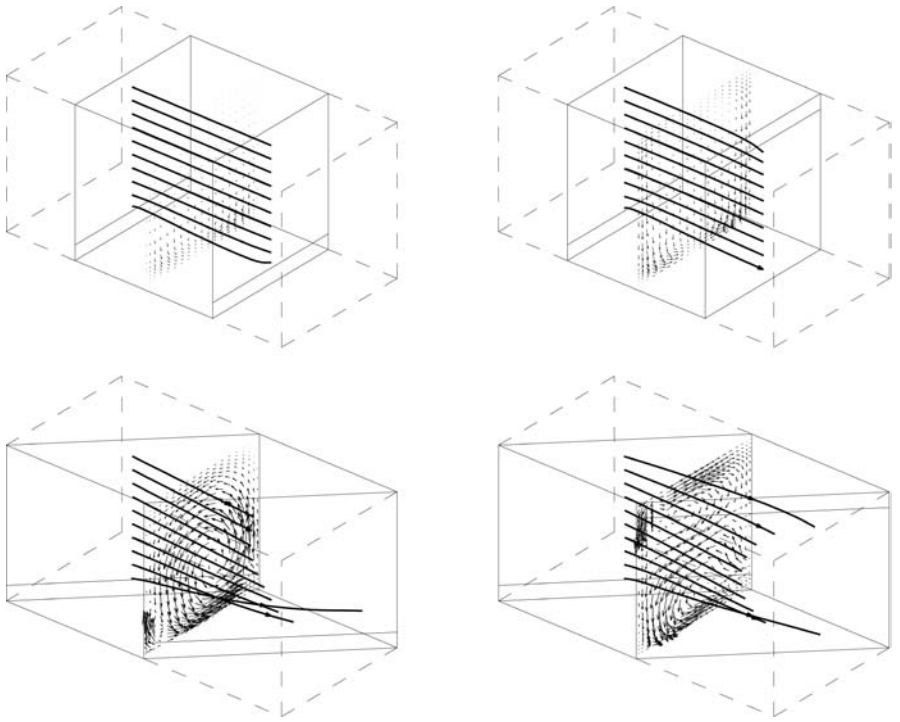

Figure 11.
Ribbed square channels: trajectories and transverse velocity vectors at Re = 300 with 90° and 45° ribs (one-sided ribs on the left; staggered ribs on the right)

longitudinal vortex and, practically, no mixing between near-wall and centre flows. Transverse ribs induce transverse vortices that, in stationary flows, are not effective as mixing promoters.

The quantitative findings concerning pressure drop and heat transfer rates in ribbed channels are reported in Figure 12 for different Reynolds numbers, up to the critical value. In this figure, the Nu and f values pertaining to fully developed flow and thermal fields in ribbed square channels have been divided by the corresponding values for smooth square channels ($Nu_0 = 2.976$ and $f_0 = 14.227/Re$) reported by Shah and London (1978, p. 200). As could have been inferred from the previous qualitative discussion, only ribs that are both staggered and angled have a beneficial effect on the heat transfer rate, even if all rib configurations increase pressure losses. In fact, values of Nu/Nu_0 (denoted by square symbols) increase steadily with Re only if ribs are both staggered and angled. On the contrary, values of f/f_0 (denoted by triangular symbols) increase steadily with all rib configurations.

Finally, it can be observed that, also in ribbed channels, flows become unsteady above the critical value of the Reynolds number. The direct calculation of the critical Reynolds number is a difficult task, because transients become longer and longer as one approaches the critical point, and the amplitude of the oscillations tends to zero. The values of Table I refer to

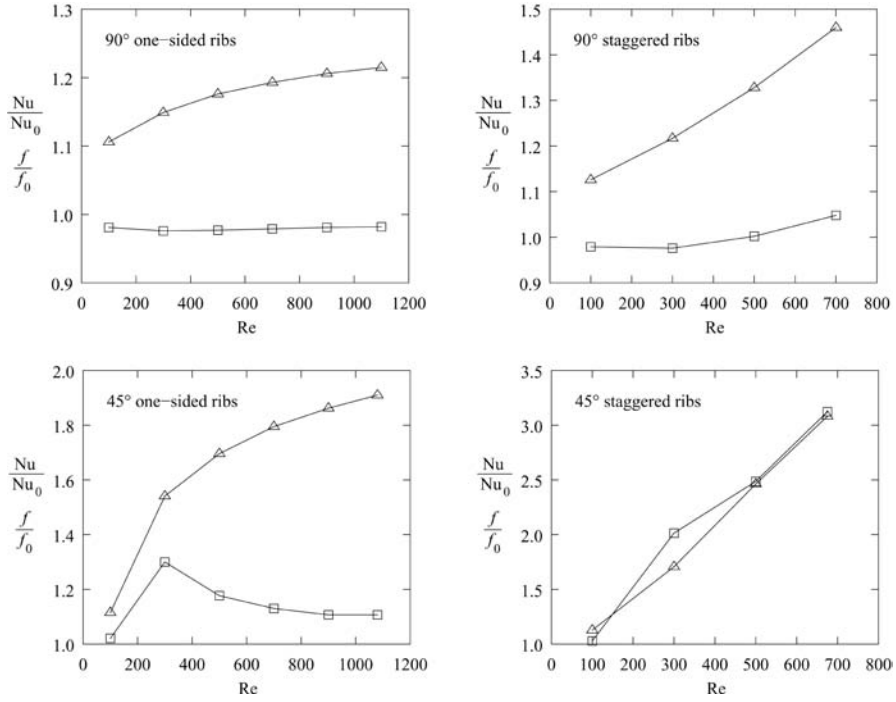

Figure 12.
Ribbed square channels: apparent friction factors (triangles) and average Nusselt numbers (squares) for $Re < Re_{cr}$, normalized with corresponding values for smooth square channels

Table I.
Approximate values of the critical Reynolds number in ribbed square channels

Rib angle (°)	One-sided ribs	Staggered ribs
90	>1,100	> 700
60	860	615
45	1,080	675

flow conditions slightly above critical and have been found by trial-and-error. It is interesting to note that the strength of longitudinal vortices influences the value of the critical Reynolds number. In fact, Re_{cr} first decreases with decreasing rib angles, because longitudinal vortices destabilize transverse vortices. On the contrary, below a certain value of the angle, Re_{cr} increases with decreasing rib angles, because the strength of transverse vortices tends to zero for ribs aligned with the main flow.

Conclusions

Convection enhancing devices fall within three main categories: surface interruptions, transverse vortex generators and longitudinal vortex generators. Surface interruptions and transverse vortex generators can be investigated in

the context of two-dimensional schematizations, while longitudinal vortex generators require three-dimensional analyses. Irrespective of the geometry, the flow becomes time dependent above a critical value of the Reynolds number. Then, the effects of vortex shedding and the associated flow unsteadiness can be captured only by solving the unsteady Navier-Stokes and energy equations.

Surface interruptions prevent the continuous growth of boundary layers by periodically interrupting them. Transverse vortices always increase pressure losses, but enhance convection only above the critical value of the Reynolds number, when vortex shedding brings fresh fluid from the main stream to the wall surfaces. On the contrary, longitudinal vortex generators can be effective even in stationary flows.

References

Ali, M.M. and Ramadhyani, S. (1992), "Experiments on convective heat transfer in corrugated channels", *Experimental Heat Transfer*, Vol. 5, pp. 175-93.

Cheung, C.H. and Huang, W.H. (1991), "Numerical prediction for laminar forced convection in parallel-plate channels with transverse fin arrays", *Int. J. Heat Mass Transfer*, Vol. 34, pp. 2739-49.

Comini, G. and Croce, G. (2001), "Convective heat and mass transfer in tube-fin exchangers under dehumidifying conditions", *Numerical Heat Transfer, Part A*, Vol. 40, pp. 579-99.

Comini, G., Nonino, C. and Savino, S. (2002), "Convective heat and mass transfer in wavy finned-tube exchangers", *International Journal of Numerical Methods for Heat and Fluid Flow*, Vol. 12, pp. 735-55.

Fiebig, M. (1996), "Vortices: tools to influence heat transfer – recent developments, in Celata, G.P., Di Marco, P. and Mariani, A. (Eds), *2nd European Thermal Sciences and 14th UIT National Conference*, ETS, Pisa, Italy, Vol. 1, pp. 41-56.

Fiebig, M. and Mitra, N.K. (1998), "Experimental and numerical investigation of heat transfer enhancement with wing-type vortex generators", in Sundén, B. and Faghri, M. (Eds), *Computer Simulation in Compact Heat Exchangers*, Computational Mechanics Publications, Southampton, pp. 227-54.

Gambolati, G. (1988), *Elements of Numerical Analysis* (*in Italian*), Libreria Cortina, Padova, Italy.

Heikal, M.R., Drakulic, R. and Cowell, T.A. (2000), "Multi-louvered fin surfaces", in Sundén, B. and Eggs, P.J. (Eds), *Recent Advances in Analysis of Heat Transfer for Fin-Type Surfaces*, WIT Press, Southampton, pp. 211-50.

Howard, D., Connolley, W.M. and Rollett, J.S. (1990), "Unsymmetric conjugate gradient methods and sparse direct methods in finite element flow simulations", *Int. J. Numer. Meth. Fluids*, Vol. 10, pp. 925-45.

Kays, W.M. and London, A.L. (1984), *Compact Heat Exchangers*, McGraw-Hill, New York, pp. 156-61.

Kelkar, K.M. and Patankar, S.V. (1987), "Numerical prediction of flow and heat transfer in a parallel plate with staggered fins", *ASME J. Heat Transfer*, Vol. 109, pp. 25-30.

Kukreja, R.T., Lau, S.C. and McMillin, R.D. (1993), "Local heat/mass transfer distribution in a square channel with full and V-shaped ribs", *Int. J. Heat Mass Transfer*, Vol. 36, pp. 2013-20.

Lopez, J.R., Anad, N.K. and Fletcher, L.S. (1996), "Heat transfer in a three-dimensional channel with baffles", *Numerical Heat Transfer, Part A*, Vol. 30, pp. 189-205.

Nonino, C. and Comini, G. (1997), "An equal order pressure-velocity algorithm for incompressible thermal flows – Part 1: formulation", *Numerical Heat Transfer, Part B*, Vol. 32, pp. 1-15.

Nonino, C. and Comini, G. (1998), "Finite-element analysis of convection problems in spatially periodic domains", *Numerical Heat Transfer, Part B*, Vol. 34, pp. 361-78.

Nonino, C. and Comini, G. (2002), "Convective heat transfer in ribbed square channels", *International Journal of Numerical Methods for Heat and Fluid Flow*, Vol. 12, pp. 610-28.

Nonino, C., Comini, G. and Croce, G. (1999), "Three-dimensional flows over backward facing steps", *International Journal of Numerical Methods for Heat and Fluid Flow*, Vol. 9, pp. 224-39.

Patankar, S.V., Liu, C.H. and Sparrow, E.M. (1977), "Fully developed flow and heat transfer in ducts having streamwise-periodic variations of cross-sectional area", *Trans. ASME, J. Heat Transfer*, Vol. 99, pp. 180-6.

Shah, R.K. and Bhatti, M.S. (1987), "Laminar convective heat transfer in ducts", in Kakac, S., Shah, R.S. and Aung, W. (Eds), *Handbook of Single-Phase Convective Heat Transfer*, Chapter 3, Wiley, New York, NY.

Shah, R.K. and London, A.L. (1978), "Laminar flow forced convection in ducts", *Advances in Heat Transfer*, Supplement 1, Academic Press, New York, NY.

Sundén, B. (1999), "Enhancement of convective heat transfer in rib-roughened rectangular ducts", *Enhanced Heat Transfer*, Vol. 6, pp. 89-103.

Webb, R.L. (1987), "Enhancement of single phase heat transfer", in Kakac, S., Shah, R.S. and Aung, W. (Eds), *Handbook of Single-Phase Convective Heat Transfer*, Chapter 17, Wiley, New York, NY.

Webb, R.L. (1994), *Principles of Enhanced Heat Transfer*, Wiley, New York, NY, pp. 87-124.

Webb, B.W. and Ramadhyani, S. (1985), "Conjugate heat transfer in a channel with staggered ribs", *Int. J. Heat Mass Transfer*, Vol. 28, pp. 1679-87.

Zhang, L.W., Balachandar, S., Tafts, D.K. and Najjar, F.M. (1997), "Heat transfer enhancement mechanisms in inline and staggered parallel-plate fin heat exchangers", *Int. J. Heat Mass Transfer*, Vol. 40, pp. 2307-25.